APPLIED SCIENCES AND ENGINEERING

Ultralow power artificial synapses using nanotextured magnetic Josephson junctions

Michael L. Schneider,* Christine A. Donnelly, Stephen E. Russek, Burm Baek, Matthew R. Pufall, Peter F. Hopkins, Paul D. Dresselhaus, Samuel P. Benz, William H. Rippard

Neuromorphic computing promises to markedly improve the efficiency of certain computational tasks, such as perception and decision-making. Although software and specialized hardware implementations of neural networks have made tremendous accomplishments, both implementations are still many orders of magnitude less energy efficient than the human brain. We demonstrate a new form of artificial synapse based on dynamically reconfigurable superconducting Josephson junctions with magnetic nanoclusters in the barrier. The spiking energy per pulse varies with the magnetic configuration, but in our demonstration devices, the spiking energy is always less than 1 aJ. This compares very favorably with the roughly 10 fJ per synaptic event in the human brain. Each artificial synapse is composed of a Si barrier containing Mn nanoclusters with superconducting Nb electrodes. The critical current of each synapse junction, which is analogous to the synaptic weight, can be tuned using input voltage spikes that change the spin alignment of Mn nanoclusters. We demonstrate synaptic weight training with electrical pulses as small as 3 aJ. Further, the Josephson plasma frequencies of the devices, which determine the dynamical time scales, all exceed 100 GHz. These new artificial synapses provide a significant step toward a neuromorphic platform that is faster, more energy-efficient, and thus can attain far greater complexity than has been demonstrated with other technologies.

INTRODUCTION

Recently, neuromorphic computing has been demonstrated in a number of hardware platforms, including modified complementary metal-oxide semiconductor (CMOS) architectures (1), static random-access memory–type synapses with CMOS neurons (2), and memristive synapses with CMOS neurons (3). These implementations have demonstrated significant improvements in efficiency compared to software neural networks run on CMOS platforms using a standard von Neumann architecture, and yet, all of these implementations are orders of magnitude less efficient than the human brain (2). The synapse is widely believed to be integral for both learning and memory (4). With approximately 10^{15} synapses in the human brain, it is a critical component of neural circuitry. Hence, finding a simple, low-energy, artificial synapse is an important step in making a neuromorphic computer that can approach the level of complexity of the human brain. The potential gains from neuromorphic computing have led to intense research in devices that can mimic the functionality of a synapse (5–12). Here, we demonstrate a new physical implementation of an artificial synapse that is orders of magnitude more efficient than that of a human brain, with a spiking energy that is sub-attojoule per synaptic event.

These new artificial synapses are compatible with single flux quantum (SFQ) Josephson junction (JJ) circuits that can provide the underlying technology platform needed to scale large neuromorphic systems (13–16). On the basis of the Josephson effect (17), a JJ can produce fast, low-voltage spikes of a few picoseconds in duration when the current through the junction exceeds its critical current I_c (13). These SFQ spikes have a time-integrated voltage amplitude given by the flux quantum $\Phi_0 = 2.068 \times 10^{-15}$ V·s. With its intrinsic spiking behavior, neuromorphic SFQ circuitry has been proposed and demonstrated at a basic level (18–23). A missing component of these neuromorphic systems has been a compact low-energy plastic synapse analog. Here, we demonstrate a synaptic element based on a dynamically reconfigurable JJ synapse capable of non-Hebbian learning (4, 24). We also

National Institute of Standards Technology, Boulder, CO 80305, USA.
*Corresponding author. Email: michael.schneider@nist.gov

demonstrate the basic energy and size scaling behavior required to realize a low-power, complex neuromorphic system based on these artificial synapses combined with SFQ neurons.

RESULTS

In its most basic form, an artificial synaptic element acts to weight the input and output signals to and from neuronal elements. In the human brain, this is accomplished, in part, by long-term changes in the quantity of neurotransmitter vesicles and the number of neurotransmitter receptors (4). For example, a synaptic connection would be strengthened if the number of receptors in the postsynaptic dendrite was increased. The artificial synapse demonstrated below is composed of a JJ barrier that contains Mn nanoclusters and superconducting Nb electrodes. Each of these clusters has a net spin alignment. By aligning the net spins of several clusters, we increase the overall magnetic order in the JJ synapse, which tunes the critical current of that synapse. By changing the critical current of the JJ synapse, we can change the connection strength between two neuronal SFQ elements. Figure 1A shows a schematic of a JJ synapse in the strong and weak weighting configurations. The amount of magnetic order between the clusters is analogous to the number of neurotransmitter receptors in the biological system.

Superconducting properties of the JJ synapse

To understand the dynamic range of the JJ synapse and thus its potential range of weighting values, the superconducting critical current must be characterized as a function of the magnetic nanocluster configurations. These device transport measurements for a 10-μm circular JJ synapse are shown in Fig. 1 (B and C). The device voltage versus current for a JJ synapse in the disordered magnetic state is shown in Fig. 1B. The relatively large value of the superconducting critical current corresponds to a strong synaptic weighting value. The data (blue circles) are well fit by a standard RSJ model (25), with a critical current of 1.30 ± 0.02 mA and a normal state resistance of 1.32 ± 0.02 milliohm. The dc voltage measured here is the time average of the spiking state of the JJ synapse. When the superconducting

critical current is exceeded, the device leaves the superconducting state and enters the voltage state, where it starts emitting SFQ pulses. The bottom inset in Fig. 1B shows a device simulation displaying the spiking behavior, which gives the measured average voltage-current characteristic upon time averaging.

The magnetic ordering of the nanoclusters of a JJ synapse can be increased by applying current pulses in an applied magnetic field, which will lower the synaptic weighting value of the devices. To increase the synaptic weight, one must decrease the magnetic order in the barrier, which can be accomplished by applying electrical pulses in a zero field. The high synaptic weight state (low magnetic order) of a 10-μm circular JJ synapse is shown in Fig. 1B. The application of a 5-mT static field alone does not change the magnetic order in the artificial synapse. However, the combination of electrical pulses in an external 5-mT magnetic field sets the device into the low synaptic weight state (that is, magnetically ordered) (Fig. 1C). In this example, the ordering was carried out with 11 electrical pulses of about 4 pJ and 1 ns in duration. In the magnetically ordered state, there is a substantial decrease in the superconducting critical current, $I_c = 0.08 \pm 0.02$ mA, while the same approximate normal state resistance of 1.30 ± 0.02 milliohm is maintained.

To scale the devices to a size below 100 nm, the observed change in I_c and, thus, the synaptic weight would ideally be the result of the interaction between the superconducting and magnetic order parameters

(26), as opposed to the result of a stray field from the barrier on the superconducting electrodes. We verify that this is the dominant mechanism for the change in I_c in the JJ synapses. A JJ with a uniform barrier leads to a Fraunhofer diffraction pattern of the superconducting order parameter (as measured by the JJ critical current I_c) as a function of an applied magnetic field (27). For circular JJ synapses in the disordered and partially ordered states, the critical current versus applied field data can be fit to an Airy function. Figure 1D shows the I_c versus applied field data from a 10-μm-diameter JJ synapse for four different levels of magnetic order. The data are presented in a waterfall plot, with each magnetically less ordered data set being offset by +0.3 mA relative to the previous data set. The solid lines through the data points in Fig. 1D are fits to the Airy function, as expected for circular junctions. In the most disordered state (blue), there is a shift of the central peak of -0.36 ± 0.04 mT. This implies that some overall magnetic order even in this "disordered" state remains (28). The magenta, black, and red data show further ordering of the same device. The side lobes do not fit the Airy function well, indicating that the current flow through the junction is nonuniform for those applied fields. This is likely the result of local magnetic order in the magnetic nanoclusters (29). The reduction in amplitude of the main peak of the Fraunhofer patterns indicates that the dependence of I_c on magnetic order is due to the interaction between the superconducting order parameter and the net spin ordering of the nanoclusters in the JJ synapse. Therefore, the devices should not lose their wide synaptic weight range when scaled to much smaller sizes.

Device operation and scaling

A demonstration of a potential scheme to change the synaptic weighting via changing magnetic order using electrical current pulses is shown in Fig. 2A for a 10-μm-diameter JJ synapse. Starting in a disordered state with high synaptic weight, the net Mn nanocluster spins are increasingly ordered using 70-ps rise time and 242-ps duration, 11-pJ current pulses that are applied in a 20-mT magnetic field. The value of I_c is reduced in a relatively continuous manner, as is desired for variable weight tuning of a synapse. We expect that given enough pulses, the trend in Fig. 2A will eventually saturate to the minimum value of about 10 μA. The slow variation in I_c with a larger number of pulses will be useful in architectures where the synapse is undergoing online learning and where small changes of synaptic weight are desired for any given pulse. In the case of an architecture with an initial training phase, after which the operating pulses are not desired to alter the synaptic weight, a larger pulse energy could be used to markedly speed up the process. The energy required to
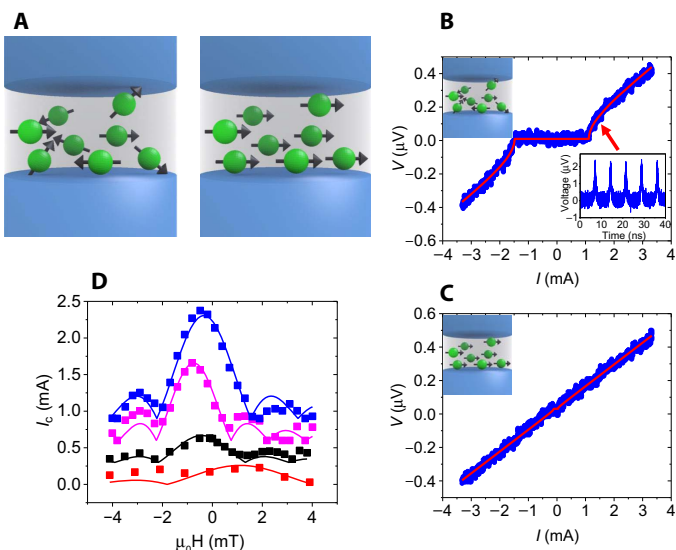

Fig. 1. Spin-dependent superconducting transport. (**A**) Schematic of the JJ synapse in the magnetically disordered state (left) and the magnetically ordered state (right). (**B**) Data (blue circles) and fit to the resistively shunted junction (RSJ) model (red line) of the voltage-current characteristic taken at 4 K on a 10-μm-diameter JJ synapse in the disordered state. The data are well fit with an RSJ shown in red. Lower inset: Simulated voltage spike train above I_c; the average of the spike train results in the measured quasi-static voltage measured. Upper inset: Schematic showing the magnetically disordered state of the junction for this measurement. (**C**) Data (blue circles) and fit to the RSJ model (red line) of the voltage versus current characteristic taken at 4 K on the same 10-μm-diameter JJ synapse in the ordered state. Inset: Schematic showing the magnetically ordered state of the junction for this measurement. (**D**) Fraunhofer diffraction of the same JJ synapse in varying magnetic ordered states. The most ordered state is in red, disorder is increased for black and magenta, and most disordered data are in blue. Black data are offset by 0.3 mA, magenta data are offset by 0.6 mA, and blue data are offset by 0.9 mA. Data are shown as squares with fits to the Airy function shown as lines.
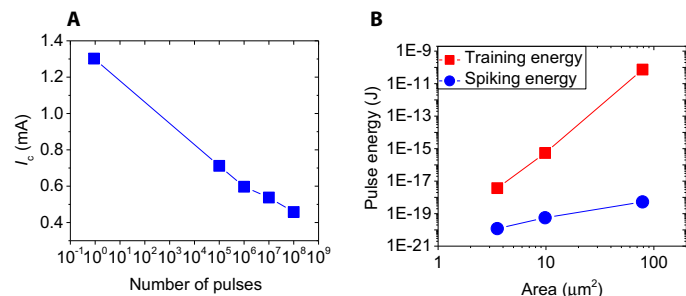

Fig. 2. Device operation and scaling. (**A**) Critical current measured in a zero field after the application of electrical ordering pulses (ordering pulses were applied in a 20-mT magnetic field); the line serves as a visual guide. (**B**) Electric pulse energy required to magnetically order the JJ synapse in a 20-mT applied magnetic field (red squares) and SFQ pulse energy (blue circles) versus JJ synapse cross-sectional area.

change the magnetic order of the devices is more efficient than a simple joule heating mechanism. In the case of Fig. 2A, if all the energy in these current pulses went into heating the junction, we would expect a roughly 15-K temperature increase, which is below the 52-K magnetic blocking temperature of this device. This implies a direct interaction between the spin clusters and the current, an effect that becomes more pronounced for the smaller device sizes shown below.

Reducing the size of the JJ synapse should also reduce the total energy per pulse required to change the magnetic order. This general size-energy scaling behavior for single pulse ordering can be seen in Fig. 2B. In the smallest JJ synapses, with an elliptical cross section of 1.5 μm × 3.0 μm, the energy required to order the magnetic clusters is 3 aJ, excluding the energy required to supply the 20-mT external field. Note that these synapses operate at 4 K, and thus, a neuromorphic system based on this technology has an additional cooling overhead. Typically for larger-scale systems, one can cool 1 W at 4 K using 1 kW of power (30). Even considering this overhead for cooling, large-scale systems of JJ synapses with 10^{18} synaptic events per second will be more energy-efficient than either CMOS or biological systems with a clear path to further lower the energy by reducing the JJ synapse size. It should also be noted that 3 aJ is the energy required to tune the JJ synapse. The energy per synaptic spike (the mechanism of information transfer during real-time operation of a neural system) is given by the SFQ pulse energy $\sim I_b \Phi_0$ (31). This energy is lower than that of the magnetic cluster ordering for these JJ synapses. Figure 2B shows the size-energy scaling for both JJ synapse tuning (red squares) and synaptic spiking (blue circles). The data in blue are the calculated pulse energies $\sim I_c \Phi_0$ at the maximum I_c of the JJ synapses (13). We find that both the energy required to order the magnetic clusters and the operating pulse energy are reduced as the device size is decreased. It is not understood why the training energy is reducing so rapidly with the device diameter. We speculate that it may be the result of nonuniform current density during the application of the training pulses in the larger devices. The pulse energy of the JJ synapse sets the energy scale for circuit operation. Digital SFQ circuits typically target critical currents of no less than 100 μA because unintended pulsing from thermal energy must be controlled precisely to maintain extremely low error rates (13). However, in neuromorphic circuits, stochastic firing of the JJ elements may be a desirable property (32), and this opens up the potential to reduce the operating pulse energy below 100 zJ. In addition, depending on the architecture chosen, it may be desirable to have the synaptic weights modified using the operating pulse energy (for example, in the case of Hebbian learning). Figure 2B suggests that scaling to smaller-size junctions may be a way to enable this type of synaptic weight training paradigm in neuromorphic JJ circuits. Using the devices currently demonstrated, one could make a direct hardware implementation of a neural network where the weights of the JJ synapses are set initially before operation. Further tuning of the synaptic weights could be performed during a nonoperational phase. With additional circuitry to provide pulses with sufficient energy to reorient the magnetic clusters, more frequent weight tuning could be implemented during an update step.

Magnetic JJs based on continuous ferromagnetic films designed for cryogenic memory applications have already been demonstrated with cross sections as small as 50 nm × 100 nm (26). With the reduction in Mn cluster size and barrier thickness, we expect that the neuromorphic technology should be able to reach similarly small sizes. It would also significantly reduce the complexity of design for neuromorphic JJ synapse systems if no magnetic field control lines were needed to order the JJ synapses. The orientation of the ferromagnet in a magnetic JJ, for use in cryogenic memories, can be manipulated using spin transfer torques (26, 33–36), which allow the devices to attain the ordered (parallel) state and the disordered (antiparallel) state without the use of external fields. Incorporating similar polarizing structures in the JJ synapse is a promising avenue for the elimination of magnetic field control lines while still maintaining the full dynamic range of the JJ synapse.

Device modeling

Large-scale neural circuits will require the ability to model individual circuit elements and require layout tools and electronic design automation for circuit modeling. We have developed circuit models of the JJ synapses in Verilog and ported them into a version of SPICE suitable for SFQ circuit modeling. A modified version of the resistively and capacitively shunted junction (RCSJ) model (27) was used to simulate the reconfigurable JJ synapses. The dynamical equations of a JJ, in the simplest model, are isomorphic to that of a forced damped pendulum. An SFQ pulse, our synthetic neural spike, corresponds to one revolution of the pendulum, overcoming a potential energy barrier of $I_c \Phi_0 / 2\pi$. The spiking rate is dependent on the energy barrier, the input current, and the device temperature. One can calculate the Josephson plasma frequency in this model as $\omega_p = \sqrt{2\pi I_c / \Phi_0 C}$, where C is the capacitance of the junction. Using the values for the 1.5 μm × 3.0 μm junctions demonstrated above, we estimate that the natural frequency of these junctions would be 170 GHz. This natural frequency would allow for very-high-speed implementations of neuromorphic systems based on the JJ synapse.

The dynamical equations of a JJ synapse are similar to those for a standard JJ, except that the JJ synapse device parameters, such as critical current, are dependent on the internal magnetic structure characterized with a magnetic order parameter, $m = \frac{1}{M} \sum_i \vec{m}_i$, where $\vec{m}_i$ are the moments of each Mn cluster and M is the total moment of all clusters. The effect of the magnetic order parameter m should be governed by the superconducting proximity effect in ferromagnetic metals (37–39). We would expect that the ordering of the magnetic clusters should be analogous to changing the thickness of the ferromagnetic layer. Thus, the variation of I_c could be quite complex and nonmonotonic. We expect that with proper materials tuning, we can fabricate JJ synapses with electrical parameters such that I_c will be reduced in an approximately linear manner with increasing magnetic order. We model this behavior as

$$I_c(m, T) = ((1 - m)I_{cv} + I_{cm})\left(1 - \left(\frac{T}{T_c}\right)^2\right) \qquad (1)$$

where I_{cv} is the portion of the critical current that changes with the magnetic state, I_{cm} is the minimum critical current in the totally ordered magnetic state, T is the device temperature, and T_c is the superconducting critical temperature. In the model used for this work, $I_{cv} = 8$ μA and $I_{cm} = 2$ μA, corresponding to a 10-μA maximum critical current achieved when $m = 0$ (disordered state) and $T = 0$. The magnetic order parameter varies with the integrated junction voltage as $dm \propto V(t)dt$ between $m = 0$ and $m = 1$; that is, a voltage pulse across the junction causes the order parameter to increase and critical current to decrease up to a saturation point.

The circuit schematic that was used to test the basic neuromorphic circuit element, demonstrating the functionality of the JJ synapse, is shown in Fig. 3A. A standard dc bias to SFQ pulse JJ (14) used to represent the output of a presynaptic neuron is shown in blue. This JJ
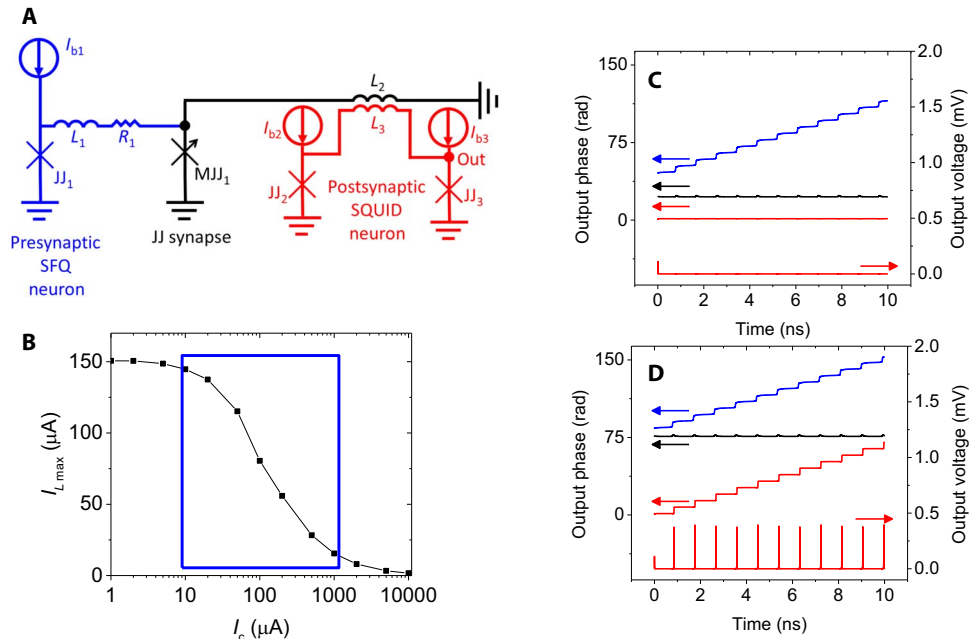
Fig. 3. JJ synapse SPICE simulation. (**A**) Circuit diagram used in the simulation, where I_c of $JJ_1 = JJ_2 = JJ_3 = 200$ μA, $L_1 = L_3 = 3$ pH (picohenry), $L_2 = 5$ pH, and $R_1 = 100$ milliohm. (**B**) Peak current through the coupling inductor L_2 versus I_c of the MJJ. I_c values within the blue box are those measured in a single MJJ. (**C**) Circuit operation with low magnetic order $I_c = 100$ μA (low synaptic weight) showing the phase modulation of the presynaptic (input) JJ (blue), the JJ synapse (black), the postsynaptic (output) JJ (red), and the output voltage (red right axis). (**D**) Circuit operation with high magnetic order $I_c = 50$ μA (high synaptic weight) showing the phase modulation of the presynaptic (input) JJ (blue), the JJ synapse (black), the postsynaptic (output) JJ (red), and the output voltage (red left axis).

provides the input pulses for the circuit. A 100-milliohm resistor R_1 was used to minimize any flow of dc current from the presynaptic neuron's bias source into the following JJ synaptic element. R_1 not only prevents the dc bias current from flowing to the synaptic magnetic JJ (MJJ) but also breaks the superconducting loop (JJ_1, L_1, and L_2), preventing the accumulation of the flux in the loop, which would lead to the eventual stoppage of operation. The flux will leak out from the loop through R_1 with a resistor-inductor time constant. Thus, the maximum frequency of pumping fluxons in this circuit is set by this time constant and can be controlled with I_{b1} current. The current parameters maintain a system balance and operation up to a gigahertz scale. The JJ synapse element acts to weight the pulses from the presynaptic neuron (shown in black). Here, we use the variable Josephson inductance (25), which in the small current limit, is proportional to $1/I_c$ as a means to split the incoming current pulse. This synaptic circuit element can then be roughly viewed as two inductors in parallel, with the current through each inductive branch determined by the critical current of the JJ synapse. Figure 3B shows the peak current through the inductor L_2 as a function of the critical current of the JJ synapse for an input pulse with 150-μA peak current. The range of critical currents within the blue box represents the range that we have demonstrated in a single JJ synapse, as discussed above.

Mutual inductance, with a coupling efficiency of 50%, is used to couple the pulse from the synaptic stage at L_2 to the output stage via L_3. The postsynaptic output neuron is modeled as a superconducting quantum interference device (SQUID). The junctions in the output SQUID are designed to have a fast response time compared to the pulse width of the coupled input flux. In this regime, the output device behaves similarly to a dc-to-SFQ converter (13), with the net coupled flux bias from one or multiple input synapses serving as its "dc" input. When the amplitude of the net input flux bias pulse exceeds a threshold,

the junctions in the output SQUID sequentially undergo 2π phase slips as the flux bias rises above, and then falls back below, this threshold. In a larger circuit, we would envision multiple synchronous synaptic inputs coupled to a single large-inductance output SQUID stage (40). The output pulse produced at this stage could then be further connected to subsequent neural network layers.

Figure 3C shows the output of the three main elements for the case of a low synaptic weight, which is implemented with high $I_c = 100$ μA that can be achieved by disordering the magnetic state. The presynaptic JJ neuron undergoes 2π phase slips (shown in blue) because its input current is in the "on" state. Although the phase of the JJ synapse also shows some small phase variation, it does not continuously evolve and does not undergo any 2π phase slips. The JJ synapse retains this small-signal behavior over the course of the input pulse, even when I_c is suppressed, partly because the characteristic response time of the MJJs increases as their I_c decreases. As a result, no 2π phase slips were observed from this JJ over the entire range (Fig. 3B) of critical currents tested. The output is shown as the phase and voltage of a JJ in the output SQUID, labeled in Fig. 3A. Thus, as desired in the case of low synaptic weight, no phase evolution of the output JJ was observed even when the presynaptic neuron is firing.

Figure 3D shows the output of the three main elements for the case of high synaptic weight, which is implemented with low $I_c = 50$ μA that can be achieved by ordering the magnetic state. Again, the presynaptic JJ neuron undergoes 2π phase slips (shown in blue) because its input current is in the "on" state. The phase of the JJ synapse again shows some small phase variation but does not continuously evolve because it does not undergo any 2π phase slips, as desired. However, in this case, the peak current through the coupling inductor L_2 is increased (Fig. 3b) because the low I_c MJJ has a larger inductance, and the resulting peak flux bias through the output stage causes an output SFQ pulse. This can

be observed in the phase evolution of the output JJ and the corresponding output voltage pulses.

Stochastic modeling

Stochasticity mimics natural brain operation and has been shown to benefit learning algorithms in deep neural networks (32). Because we can operate near the thermal stability limit of the JJ synapse, we can induce variable amounts of stochasticity in our circuits by elevating the temperature. We define the stochasticity as $1/\delta$, where $\delta = \frac{\phi_0 I_c}{2\pi k_B T}$ is the thermal stability given by the ratio of the spiking energy barrier to the thermal energy. Here, k_B is the Boltzmann constant, and T is the temperature in kelvins. For stochasticity values of less than one, the dynamics are basically deterministic, whereas when the stochasticity is greater than one, there is a significant stochastic component. Given the large nonlinear variation of I_c with temperature near the superconducting critical temperature T_c, we can expect to be able to vary $1/\delta$ over a wide range by adjusting the temperature over just a few degrees, thereby controlling the amount of stochasticity in the neural circuit. We find that there is a smooth nonlinear variation of the I_c as a function of temperature in the partially ordered state of a 10-μm JJ synapse, as shown in Fig. 4A. On the right axis of Fig. 4A, we plot $1/\delta$ for a simulated device with a diameter of 100 nm to show the large range of potentially available stochasticity in smaller devices.

To investigate the potential advantages of stochastic neuromorphic SFQ circuits, we have developed a SPICE model that includes thermal fluctuations. Specifically, an additional current branch is added to our modified RCSJ model to account for "white noise" current fluctuations. Theoretically, the thermal fluctuations have constant power spectral density, given by the Johnson-Nyquist formula as $S_I(f) = \frac{4k_B T}{R_N}$. As the

thermal stability ratio δ becomes smaller, the probability for a JJ to temporarily bias into the voltage state and emit an SFQ pulse becomes larger.

Figure 4B shows a block diagram of the circuit that we modeled to understand the influence of thermal noise on JJ synapses. In these simulations, the magnetic order parameter varies from $m = 0$ to $m = 1$ within 100 SFQ voltage pulses, and we monitor the spiking rate output by a JJ synapse. Given a certain input current, a reconfigurable JJ synapse will generate SFQ voltage spikes at a rate nonlinearly dependent on I_c, which is dependent on the history of input spikes, the input current, and device temperature (41). The JJ synapse circuit, shown in Fig. 4B, was simulated at two different temperatures using the same input spike stream to show the effects of stochasticity and the dynamically reconfigurable magnetic order. At 2 K, there is no significant change in output spiking of the simulated circuit (Fig. 4C), and the simulated magnetic order parameter does not change significantly. Increasing the simulated temperature to 3 K and, thus, the stochastic energy in the JJ synapse, significantly changes both the magnetic order parameter and the output voltage spiking (Fig. 4D). In this case, the magnetic order parameter increases as it accumulates incoming spikes, which leads to more spiking activity out of the JJ synapse for the same initial input spike train.

DISCUSSION

A new type of dynamically tunable JJ has been demonstrated with potential application as a synthetic synaptic element for superconducting neuromorphic computing. In these devices, the JJ critical current, in a zero applied magnetic field, can be varied in an analog manner. Although digital implementations of JJs with magnetic barriers have
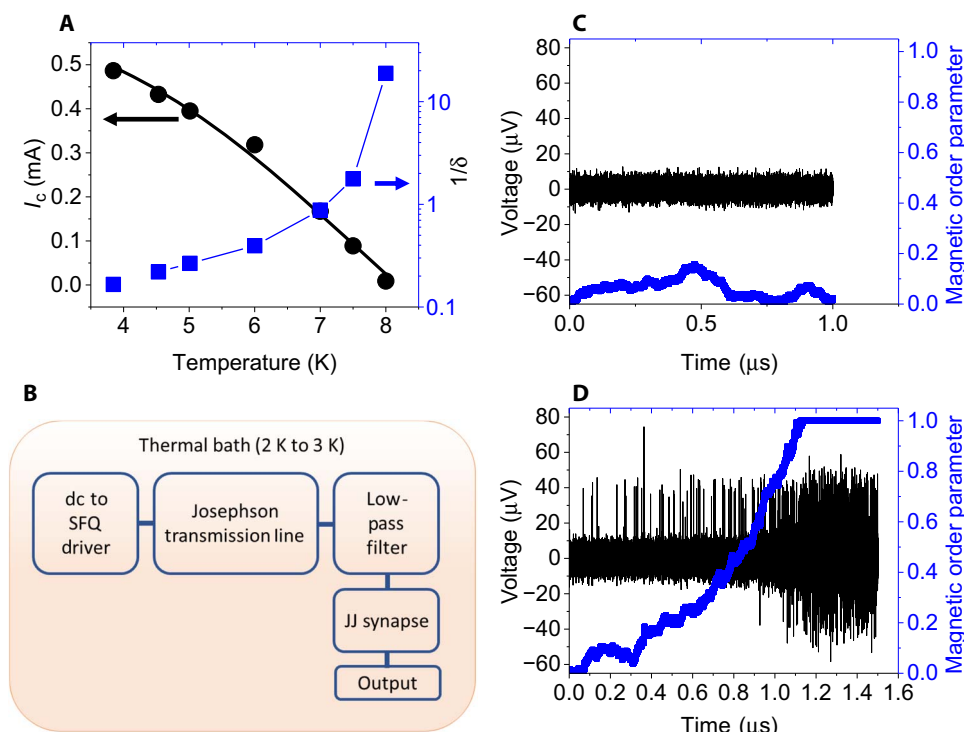

Fig. 4. SPICE simulation of stochasticity. (A) Measured critical current of a 10-μm JJ synapse in the partially ordered magnetic state as a function of temperature (black circles); lines serve as visual guides. Simulated stochasticity of a 100-nm JJ synapse as a function of temperature (blue squares). (B) Block diagram of the circuit model. (C) Voltage at output (black) and magnetic order (blue) as a function of time simulated at 2 K. (D) Voltage at output (black) and magnetic order (blue) as a function of time simulated at 3 K.
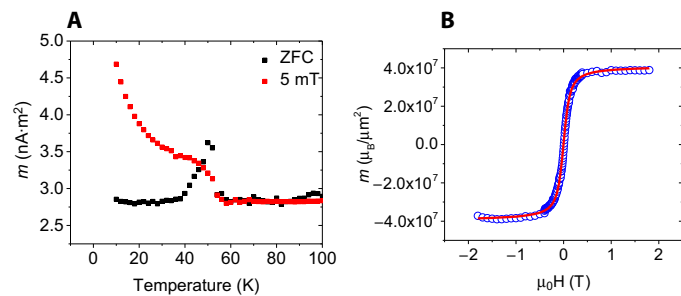
Fig. 5. Magnetic nanocluster properties. (**A**) Magnetic moment versus temperature under zero field–cooled (ZFC) (black) and field-cooled (red) conditions. The peak in the zero field–cooled curve gives a measure of the energy required to reorient the magnetic clusters. (**B**) Magnetic moment versus applied magnetic field at 70 K; data are in blue circles, and Langevin fit to the data are shown as a red line. The Langevin fit gives an estimated magnetic cluster density and moment of 2×10^4 Mn clusters/μm^2 and 2000 μ_B, respectively.

been extensively demonstrated (26, 35, 42, 43), to our knowledge, reproducible zero-field analog control has not previously been shown. The device behaves naturally as an artificial synapse that can interact with low-energy electrical pulses. There are potentially other applications of these novel JJs. For example, the low energy involved in changing the order of the magnetic clusters makes this barrier an excellent candidate for cryogenic memory applications, possibly as the magnetic free-layer material in a pseudospin-valve magnetic JJ. In addition, because of their natural spiking behavior, these devices could be used as integrate and fire neurons.

The device demonstrated here requires an external magnetic field to order the magnetic nanoclusters in the JJ synapse. One physical implementation would be to lithographically pattern magnetic field control lines above the JJ synapses. This type of implementation should work up to considerable scale, as evidenced by field-switched magnetic random-access memory products currently available with more than 1.6×10^7 bits per chip (44). However, implementations without additional field control lines would allow an even better scaling. It has previously been demonstrated that spin transfer torques can be used to switch a magnetically soft layer in a two-state JJ with a magnetic pseudospin-valve barrier (26, 35). Similar spin-polarizing layers should also allow for the elimination of a field control line in future JJ synapses. In addition, if the energy required to reorder the magnetic clusters is on the order of the SFQ pulse energy, then the JJ synapses will be capable of Hebbian learning (24). The scaling of pulse energy with device size appears to be a promising path toward realizing magnetic cluster reordering energy that will be on the order of the SFQ pulse energy.

One of the significant advantages of this system is its ability to leverage existing digital SFQ JJ logic infrastructure. Digital SFQ circuits have been demonstrated with more than 10^5 JJs (45). In addition, because of their superconducting nature, SFQ circuits can have so-called ballistic communications, both on-chip and chip-to-chip, with data transmission rates demonstrated up to 60 gigabits/s (46–48). The main advantage is that the transmission of SFQ pulses is not limited by the typical capacitive charging, which semiconductor electronics typically face. In addition, there is very little energy cost in transmitting the pulses along superconducting wires/transmission lines (30), and zero static dissipation SFQ circuits have recently been demonstrated (49). This results in the main energy dissipation mechanism as the pulse generation itself. For example, in our basic circuit element in Fig. 3, the energy dissipated for a presynaptic spike, followed by the synaptic weighting and output spike (if the synaptic weight is above threshold),

would be $\sim 3\, I_b \Phi_0 \sim 1$ aJ. The main additional cost is cooling to 4 K, which, for large-scale systems, is ~ 1000, bringing the energy required for this operation up to ~ 1 fJ. There would be an additional cost for supplying the bias currents, but these currents could be shared within each layer because they are not the tunable element. The high-speed communications could be combined with one of the many neuromorphic interconnect strategies that have been developed in CMOS, such as matrix-vector multipliers combined with thresholding (50), tree routing (51), or self-timing (52). Leveraging of fabrication tools and techniques that have been developed for CMOS and modified for both commercial magnetoresistive random-access memory and large-scale digital SFQ logic should greatly accelerated the progress of neuromorphic circuits using JJ neurons and JJ synapses. However, we should note that, although the demonstrated device and the circuit modeling are quite promising, considerable work remains to demonstrate a large neuromorphic architecture with complex layout and routing using this new technology.

MATERIALS AND METHODS
The devices were measured in a liquid He flow cryogenic probe station with a base temperature of 3.9 K and a stability of ±5 mK. The chips were thermally heat-sunk to the cold stage with an $In_{0.51}Bi_{0.325}Sb_{0.165}$ alloy. High-speed pulses were provided via microwave cables and ground-signal-ground probes. The voltage and pulse durations were taken to be the geometric mean of the pulse reduction and pulse stretching that occurred when two high-speed probes were connected via a 50-ohm impedance connection (at 4 K) using nominally identical lines on both sides. This was compared to the pulse output connected directly to a high-speed oscilloscope to determine the calibration factor, which was a 0.504 reduction in voltage and a lengthening to 242 ps for a nominal 100-ps input pulse. The current of the pulse was assumed to be that of a 50-ohm load driving a short (that is, the current was about twice that of the equivalent voltage driving a 50-ohm load). The measured device resistances varied from 1 to 100 milliohms. Given that the devices have nonzero resistance, the values quoted in the main text represent upper bounds on the currents and, thus, the energies that were calculated.

Defluxing of superconducting circuits prevents trapped flux due to persistent current loops that can distort the measurements. To remove this potentially trapped flux, the circuits were heated to 9.5 K for 2 min, above the superconducting critical temperature of the junctions and the Nb wiring, and then returned to 4 K for 3 min before measurement. The junction critical current was confirmed to be stable after the 3-min cooling wait time. Defluxing was performed after all major changes, such as contacting a device, and after any pulse larger than 100 pJ that occurred in the measurement. The critical current was confirmed to be the same before and after current pulses of less than 100 pJ before pulse experiments. In addition, defluxing was also implemented after any field ramping other than in the direct Fraunhofer patterns. Field ramps to 20 mT and back were confirmed not to change the value of I_c without the addition of a current pulse. In neuromorphic applications, all of the signal and training pulses are expected to be <<100 pJ, and any magnetic fields would be applied locally with a field control line, alleviating any need for in operando defluxing.

Magnetic barrier properties
Control of the magnetic cluster size allows one to vary the amount of energy required to adjust the weight of the artificial synapse.

With postdeposition annealing (41) or by varying the Si-Mn super-lattice spacing, one can tune the cluster size from a large number of net spins per cluster to a small number of net spins per cluster. Characterization of the clustering was carried out on blanket film stacks using a SQUID magnetometer. The blocking temperature is the temperature below which the net magnetic moments stop fluctuating on the time scale of the magnetometry measurements and give a measure of the magnetic anisotropy energy (Fig. 5A). The magnetic anisotropy energy is the energy required to reorient the spin clusters and determines how easy it is to reconfigure the magnetic order of the JJ synapses. The blocking temperature is approximated as the point in the graph (Fig. 5A) where there is a maximum in the zero field–cooled magnetic moment. This temperature also corresponds to the point in the field-cooling curve where measured magnetic moments starts to increase with decreasing temperature, which signifies the increase in the net magnetic order (53). All of the magnetic JJ synapses presented here were fabricated by sputter deposition of $Nb_{70}(Si_{0.6}Mn_{0.5}) \times 3Si_{0.6}Nb_{70}$, where the thicknesses are in nanometers. After deposition, the blanket films were annealed at 400°C for 10 min in an atmosphere of 5% H in 95% Ar and were subsequently patterned using optical lithography. One die from the device wafer was left unpatterned and was used to characterize the nanoclusters using a SQUID magnetometer. Figure 5A shows the field- and zero field–cooled data from this witness die. We found that the blocking temperature of our JJ synapses was 52 ± 2 K. The size of the Mn nanoclusters can be estimated by measuring the magnetic moment versus applied magnetic field in the paramagnetic limit, above the blocking temperature (54). Figure 5B shows magnetic moment versus applied field data taken on the same witness die at a temperature of 70 K. We fit the data (blue circles) to the Langevin functions (red line), estimating 2×10^4 Mn clusters/μm^2, with each cluster having 2000 ± 100 μ_B, where μ_B is the Bohr magneton. By reducing the cluster size, there is a clear path for reducing the pulse energy required to order/disorder the JJ synapses.

REFERENCES AND NOTES

1. A. Graves, G. Wayne, M. Reynolds, T. Harley, I. Danihelka, A. Grabska-Barwińska, S. G. Colmenarejo, E. Grefenstette, T. Ramalho, J. Agapiou, A. P. Badia, K. Moritz Hermann, Y. Zwols, G. Ostrovski, A. Cain, H. King, C. Summerfield, P. Blunsom, K. Kavukcuoglu, D. Hassabis, Hybrid computing using a neural network with dynamic external memory. *Nature* **538**, 471–476 (2016).
2. P. A. Merolla, J. V. Arthur, R. Alvarez-Icaza, A. S. Cassidy, J. Sawada, F. Akopyan, B. L. Jackson, N. Imam, C. Guo, Y. Nakamura, B. Brezzo, I. Vo, S. K. Esser, R. Appuswamy, B. Taba, A. Amir, M. D. Flickner, W. P. Risk, R. Manohar, D. S. Modha, A million spiking-neuron integrated circuit with a scalable communication network and interface. *Science* **345**, 668–673 (2014).
3. M. Prezioso, F. Merrikh-Bayat, B. D. Hoskins, G. C. Adam, K. K. Likharev, D. B. Strukov, Training and operation of an integrated neuromorphic network based on metal-oxide memristors. *Nature* **521**, 61–64 (2015).
4. P. Dayan, L. F. Abbott, *Theoretical Neuroscience* (MIT Press, 2005).
5. F. Alibart, S. Pleutin, D. Guérin, C. Novembre, S. Lenfant, K. Lmimouni, C. Gamrat, D. Vuillaume, An organic nanoparticle transistor behaving as a biological spiking synapse. *Adv. Funct. Mater.* **20**, 330–337 (2010).
6. T. Hasegawa, T. Ohno, K. Terabe, T. Tsuruoka, T. Nakayama, J. K. Gimzewski, M. Aono, Learning abilities achieved by a single solid-state atomic switch. *Adv. Mater.* **22**, 1831–1834 (2010).
7. T. Ohno, T. Hasegawa, T. Tsuruoka, K. Terabe, J. K. Gimzewski, M. Aono, Short-term plasticity and long-term potentiation mimicked in single inorganic synapses. *Nat. Mater.* **10**, 591–595 (2011).
8. A. Chanthbouala, V. Garcia, R. O. Cherifi, K. Bouzehouane, S. Fusil, X. Moya, S. Xavier, H. Yamada, C. Deranlot, N. D. Mathur, M. Bibes, A. Barthélémy, J. Grollier, A ferroelectric memristor. *Nat. Mater.* **11**, 860–864 (2012).
9. D. Kuzum, R. G. D. Jeyasingh, B. Lee, H.-S. P. Wong, Nanoelectronic programmable synapses based on phase change materials for brain-inspired computing. *Nano Lett.* **12**, 2179–2186 (2012).
10. M. D. Pickett, G. Medeiros-Ribeiro, R. S. Williams, A scalable neuristor built with Mott memristors. *Nat. Mater.* **12**, 114–117 (2013).
11. A. M. Shen, C.-L. Chen, K. Kim, B. Cho, A. Tudor, Y. Chen, Analog neuromorphic module based on carbon nanotube synapses. *ACS Nano* **7**, 6117–6122 (2013).
12. W. Xu, S.-Y. Min, H. Hwang, T.-W. Lee, Organic core-sheath nanowire artificial synapses with femtojoule energy consumption. *Sci. Adv.* **2**, e1501326 (2016).
13. K. K. Likharev, V. K. Semenov, RSFQ logic/memory family: A new Josephson-junction technology for sub-terahertz-clock-frequency digital systems. *IEEE Trans. Appl. Supercond.* **1**, 3–28 (1991).
14. P. Bunyk, K. Likharev, D. Zinoviev, RSFQ technology: Physics and devices. *Int. J. High Speed Electron. Syst.* **11**, 257–305 (2001).
15. D. K. Brock, RSFQ technology: Circuits and systems. *Int. J. High Speed Electron. Syst.* **11**, 307–362 (2001).
16. S. K. Tolpygo, V. Bolkhovsky, T. J. Weir, L. M. Johnson, M. A. Gouker, W. D. Oliver, Fabrication process and properties of fully-planarized deep-submicron Nb/Al- AlO/Nb Josephson junctions for VLSI circuits. *IEEE Trans. Appl. Supercond.* **25**, 1–12 (2015).
17. B. D. Josephson, Possible new effects in superconductive tunnelling. *Phys. Lett.* **1**, 251–253 (1962).
18. T. Hirose, T. Asai, Y. Amemiya, Pulsed neural networks consisting of single-flux-quantum spiking neurons. *Phys. C Supercond. Appl.* **463–465**, 1072–1075 (2007).
19. T. Onomi, T. Kondo, K. Nakajima, in *8th European Conference on Applied Superconductivity*, S. Hoste, M. Ausloos, Eds. (IOP Publishing Ltd, 2008), vol. 97.
20. P. Crotty, D. Schult, K. Segall, Josephson junction simulation of neurons. *Phys. Rev. E* **82**, 011914 (2010).
21. Y. Yamanashi, K. Umeda, N. Yoshikawa, Pseudo sigmoid function generator for a superconductive neural network. *IEEE Trans. Appl. Supercond.* **23**, 1701004 (2013).
22. X. Wu, J. Ma, L. Yuan, Y. Liu, Simulating electric activities of neurons by using PSPICE. *Nonlinear Dyn.* **75**, 113–126 (2014).
23. K. Segall, M. LeGro, S. Kaplan, O. Svitelskiy, S. Khadka, P. Crotty, D. Schult, Synchronization dynamics on the picosecond time scale in coupled Josephson junction neurons. *Phys. Rev. E* **95**, 032220 (2017).
24. D. O. Hebb, *The Organization of Behavior* (Wiley and Sons, 1949).
25. M. Tinkham, *Introduction to Superconductivity* (Dover, 1996).
26. B. Baek, W. H. Rippard, M. R. Pufall, S. P. Benz, S. E. Russek, H. Rogalla, P. D. Dresselhaus, Spin-transfer torque switching in nanopillar superconducting-magnetic hybrid josephson junctions. *Phys. Rev. Appl.* **3**, 011001 (2015).
27. T. Van Duzer, C. W. Turner, *Superconductive Devices and Circuits* (Prentice Hall, 1999), 458 pp.
28. C. Bell, R. Loloee, G. Burnell, M. G. Blamire, Characteristics of strong ferromagnetic Josephson junctions with epitaxial barriers. *Phys. Rev. B* **71**, 180501(R) (2005).
29. M. Weides, Magnetic anisotropy in ferromagnetic Josephson junctions. *Appl. Phys. Lett.* **93**, 052502 (2008).
30. D. S. Holmes, A. L. Ripple, M. A. Manheimer, Energy-efficient superconducting computing—Power budgets and requirements. *IEEE Trans. Appl. Supercond.* **23**, 1701610 (2013).
31. O. A. Mukhanov, Energy-efficient single flux quantum technology. *IEEE Trans. Appl. Supercond.* **21**, 760–769 (2011).
32. E. O. Neftci, B. U. Pedroni, S. Joshi, M. Al-Shedivat, G. Cauwenberghs, Stochastic synapses enable efficient brain-inspired learning machines. *Front. Neurosci.* **10**, 241 (2016).
33. J. C. Slonczewski, Current-driven excitation of magnetic multilayers. *J. Magn. Magn. Mater.* **159**, L1–L7 (1996).
34. L. Berger, Emission of spin waves by a magnetic multilayer traversed by a current. *Phys. Rev. B* **54**, 9353–9358 (1996).
35. C. Bell, G. Burnell, C. W. Leung, E. J. Tarte, D.-J. Kang, M. G. Blamire, Controllable Josephson current through a pseudospin-valve structure. *Appl. Phys. Lett.* **84**, 1153–1155 (2004).
36. L. Ye, D. B. Gopman, L. Rehm, D. Backes, G. Wolf, T. Ohki, A. F. Kirichenko, I. V. Vernik, O. A. Mukhanov, A. D. Kent, Spin-transfer switching of orthogonal spin-valve devices at cryogenic temperatures. *J. Appl. Phys.* **115**, 17C725 (2014).
37. A. I. Buzdin, Proximity effects in superconductor-ferromagnet heterostructures. *Rev. Mod. Phys.* **77**, 935–976 (2005).
38. E. A. Demler, G. B. Arnold, M. R. Beasley, Superconducting proximity effects in magnetic metals. *Phys. Rev. B* **55**, 15174–15182 (1997).
39. M. Eschrig, Spin-polarized supercurrents for spintronics. *Phys. Today* **64**, 43 (2011).
40. M. W. Johnson, P. Bunyk, F. Maibaum, E. Tolkacheva, A. J. Berkley, E. M. Chapple, R. Harris, J. Johansson, T. Lanting, I. Perminov, E. Ladizinsky, T. Oh, G. Rose, A scalable control system for a superconducting adiabatic quantum optimization processor. *Supercond. Sci. Technol.* **23**, 065004 (2010).
41. S. E. Russek, C. A. Donnelly, M. L. Schneider, B. Baek, M. R. Pufall, W. H. Rippard, P. F. Hopkins, P. D. Dresselhaus, S. P. Benz, Stochastic single flux quantum neuromorphic computing using magnetically tunable Josephson junctions, in *2016 IEEE International Conference on Rebooting Computing (ICRC)* (IEEE, 2016), pp. 1–5.

42. B. Baek, W. H. Rippard, S. P. Benz, S. E. Russek, P. D. Dresselhaus, Hybrid superconducting-magnetic memory device using competing order parameters. *Nat. Commun.* **5**, 3888 (2014).

43. M. A. E. Qader, R. K. Singh, S. N. Galvin, L. Yu, J. M. Rowell, N. Newman, Switching at small magnetic fields in Josephson junctions fabricated with ferromagnetic barrier layers. *Appl. Phys. Lett.* **104**, 022602 (2014).

44. S. Tehrani, Status and outlook of MRAM memory technology (invited), in *2006 International Electron Devices Meeting (IEDM)* (IEEE, 2006), vols. 1 and 2, pp. 330–333.

45. V. K. Semenov, Y. A. Polyakov, S. K. Tolpygo, AC-biased shift registers as fabrication process benchmark circuits and flux trapping diagnostic tool. *IEEE Trans. Appl. Supercond.* **27**, 1301409 (2017).

46. Q. P. Herr, A. D. Smith, M. S. Wire, High speed data link between digital superconductor chips. *Appl. Phys. Lett.* **80**, 3210–3212 (2002).

47. Q. P. Herr, M. S. Wire, A. D. Smith, Ballistic SFQ signal propagation on-chip and chip-to-chip. *IEEE Trans. Appl. Supercond.* **13**, 463–466 (2003).

48. Y. Hashimoto, S. Yorozu, T. Satoh, T. Miyazaki, Demonstration of chip-to-chip transmission of single-flux-quantum pulses at throughputs beyond 100 Gbps. *Appl. Phys. Lett.* **87**, 022502 (2005).

49. D. E. Kirichenko, S. Sarwana, A. F. Kirichenko, Zero static power dissipation biasing of RSFQ circuits. *IEEE Trans. Appl. Supercond.* **21**, 776–779 (2011).

50. G. Cauwenberghs, C. F. Neugebauer, A. Yariv, An adaptive CMOS matrix-vector multiplier for large scale analog hardware neural network applications, in *IJCNN-91-Seattle International Joint Conference on Neural Networks (IJCNN)* (IEEE, 1991), vol. 1, pp. 507–511.

51. P. Merolla, J. Arthur, R. Alvarez, J.-M. Bussat, K. Boahen, A multicast tree router for multichip neuromorphic systems. *IEEE Trans. Circuits Syst. I Regul. Pap.* **61**, 820–833 (2014).

52. S. B. Furber, F. Galluppi, S. Temple, L. A. Plana, The SpiNNaker project. *Proc. IEEE* **102**, 652–665 (2014).

53. M. Respaud, J. M. Broto, H. Rakoto, A. R. Fert, L. Thomas, B. Barbara, M. Verelst, E. Snoeck, P. Lecante, A. Mosset, J. Osuna, T. Ould Ely, C. Amiens, B. Chaudret, Surface effects on the magnetic properties of ultrafine cobalt particles. *Phys. Rev. B* **57**, 2925–2935 (1998).

54. J. D. Livingston, C. P. Bean, Anisotropy of superparamagnetic particles as measured by torque and resonance. *J. Appl. Phys.* **30**, S318–S319 (1959).